Sensors & Diagnostics

PAPER

View Article Online
View Journal | View Issue

Cite this: *Sens. Diagn.*, 2024, **3**, 668

The impact of analyte size on SERS enhancement location, enhancement factor, excitation wavelength, and spectrum

Yanjun Yang, [a] Xinyi Chen, [b] Bin Ai [b] and Yiping Zhao *[a]

The study systematically explores the connection between analyte particle size and the hot-spot in Au nanoparticle (NP) dimer systems. Contrary to the conventional understanding tied to localized surface plasmon resonance (LSPR), we show that depending on the analyte particle's size, the location to produce surface-enhanced Raman scattering (SERS), defined as effective hot-spot, is different from the gap based hot-spot, where the electric field reaches maximum intensity, and the corresponding resonant wavelength is also shifted significantly from LSPR wavelength. This effective hot-spot occurs primarily at the point where the Au NP contacts the analyte particle, covering a larger area than the traditional hot-spot and having a significantly smaller enhancement factor. Moreover, different effective hot-spots can be activated under various polarizations. The local electric field *versus* distance relationship decays significantly slower, complicating the interpretation of SERS spectra of large analyte particles. This complexity offers tunability, allowing for a more precise representation of unique molecular features of the analyte. Consequently, our findings demonstrate the necessity for SERS substrate design rules to be contingent on analyte particle size. Although interpreting SERS spectra is intricate, it can be refined to effectively capture distinctive molecular characteristics. These insights pave a new way to tailor SERS substrate design specifically catering to large analyte particles.

Received 11th January 2024,
Accepted 13th March 2024

DOI: 10.1039/d4sd00014e

rsc.li/sensors

1. Introduction

In recent years, surface-enhanced Raman scattering (SERS) spectroscopy has gained widespread applications in chemical and biological detection, significantly augmenting diagnostic capabilities.[1] In comparison to conventional fluorescence spectroscopy techniques commonly employed in the fields of biology and health sciences, SERS offers several distinct advantages, including enhanced sensitivity, the ability for multiplexing, chemical specificity, and a reduction in autofluorescence. Moreover, SERS enables label-free, high-resolution, and quantitative analysis, making it an invaluable tool in various applications. At the core of SERS applications lies the SERS enhancement mechanisms, particularly the electromagnetic (EM) enhancement.[2,3] This mechanism primarily arises from the formation of high-quality hot-spots within SERS-active substrates, where a substantial local electric field, generated within nanostructures by external laser excitation, is concentrated.[1–3] As long as the target molecules can adsorb onto these hot-spot locations, the SERS enhancement factor (EF) is proportionally related to $|E_{loc}/E_0|^4$, where E_{loc} and E_0 represent the magnitude of the local and incident electric fields. Consequently, the resulting SERS spectrum is dominated by the signals generated within these hot-spots. Therefore, numerous publications in SERS substrate design and mechanism explanation implement the imperative nature of identifying or designing hot-spots through diverse numerical methods.[3,4] As outlined in a recent review paper,[3] three distinct categories of hot-spots have been identified. The first-generation hot-spots encompasses individual nano-objects like Au or Ag NPs, nanorods, and nano-stars,[2] *etc.* where the side surfaces or sharp tips of these NPs serve as hot-spots. The second-generation hot-spots are characterized by controlled nanogaps resulting from the electromagnetic coupling of nano-objects, with these gaps being exceptionally narrow (≤5 nm) between two or more nano-objects. The third generation hot-spots are formed by nanogaps between nano-objects and thin films. In this case, the coupling between the EM response of the NPs and the reflected EM fields from the thin film gives rise to the EM enhancement. From a geometric perspective, these three types of hot-spots can be classified into two general configurations: the open hot-spot of a single NP system and

[a] *Department of Physics and Astronomy, The University of Georgia, Athens, GA, 30602, USA. E-mail: zhaoy@uga.edu*
[b] *School of Microelectronics and Communication Engineering, Chongqing Key Laboratory of Bio-perception & Intelligent Information Processing, Chongqing University, Chongqing, 400044, P.R. China*

the gap hot-spots, encompassing both the second- and third-generation hot-spots. If the analyte molecules are located inside the hot-spot areas, under near-resonant excitation wavelength λ_0, the substrate can produce the highest SERS signals.

However, in the context of biological-based SERS detection[5–7] or some other detections (such as microplastics),[8,9] certain target analytes possess physical dimensions comparable to or even greater than the dimensions of hot-spots. For instance, proteins like BSA typically have a nominal size of 7.1 nm,[10] viruses span diameters ranging from 20 nm to 250–400 nm (with the SARS-CoV-2 virus being approximately 100 nm in diameter),[11] bacteria exhibit considerable size of around or larger than 1 μm,[12] while microplastics shows particle size varying from tens of nanometers to a few micrometers.[13] For open hot-spots, as long as the hot-spot locations can be adsorbed on the surface of the large analyte, they can generate good SERS signal. Such a situation has been discussed in detail in ref. 14. However, for gap hot-spot, since the size (gap) of the hot-spots could be significantly smaller than the size of the analyte, the target analytes cannot physically infiltrate the hot-spot gaps or can only expose a fraction of their surface to tip-based hot-spots. Thus, the SERS signal generated from these SERS substrates for large size analytes cannot come from gap hot-spot. Though some literature has raised this issue, no systematic investigation has been done.[15–17] For example, Rastogi *et al.* used self-assembled gold nanoparticle cluster arrays to achieve impressive picomolar detection limits for both a small molecule (1-naphthalene thiol) and a large biomolecule (streptavidin, a protein) by systematically adjust the gap size of the cluster arrays.[16] Liu *et al.* applied V-shape substrate to show that the effective SERS EF decreased monotonically with the size of PMMA microsphere.[17] Several fundamental questions need to be addressed or clarified for the gap hot-spot bio-detection scenario: 1) how can one redefine an effective hot-spot (EHS) where the SERS enhancement is actually coming from when the analyte's size is comparable to or surpasses the size of conventionally defined hot-spots? 2) How does this EHS alter SERS performance, such as EF (*i.e.*, sensitivity), excitation wavelength, spectral characteristics, and others? 3) How can one comprehend the resulting SERS spectra in such a situation?

In this paper, we will define the EHS for large sized analytes in the case of gap hot-spot using an Au nanosphere dimer as an example and use finite-difference time-domain (FDTD) calculation to illustrate the impact of analyte size on SERS hot-spots and spectra. Our findings will elucidate that, for gap hot-spot SERS substrates, the EHS location and the excitation wavelength are contingent on the analyte's size. Furthermore, the SERS EF undergoes significant alterations in response to varying analyte sizes. Finally, we will demonstrate that the geometry and size of the gap hot-spot can influence the spectral shape due to the inherent heterogeneity of microorganisms.

2. FDTD calculations

A typical gap hot-spot system is a nanosphere dimer with a very narrow gap, as shown in Fig. 1, which represents a typical hot-spot configuration in SERS community.[18,19] This system is selected since it is a very simple representative of a gap hot-spot and some of the results can be easily interpreted. Since the problem we consider here is a size exclusion case, some of the results obtained here can be extended to other gap hot-spot configurations. Each sphere has the same radius R_{Au}. When the excitation laser wavelength λ_{ex} is tuned to be near the localized plasmon resonance (LSPR) wavelength λ_{LSPR} of the dimer, locations of very high local E-fields appear, and these locations are called hot-spot. Due to the shape anisotropy and plasmon hybridization, the dimer has two longitudinal LSPR modes and one transverse mode.[20] When excited near the bonding longitudinal mode ($\lambda_{ex} \approx \lambda^{b}_{LSPR}$) with a vertical polarization (V-polarization, the black arrow in Fig. 1), the hot-spot is presented in the center of the gap, *i.e.*, the **O** location (black dot in Fig. 1); when λ_{ex} is near the anti-bonding mode λ^{a}_{LSPR} with V-polarization, the hot-spots are at the two ends of the dimer along the long-axis direction, *i.e.*, **U** location (blue spot); if the excitation wavelength is near the transverse mode $\lambda_{ex} \approx \lambda^{t}_{LSPR}$ with a horizontal polarization (H-polarization, the purple arrow), the highest local E-field appears at the left and right sides of the two Au nanospheres, *i.e.*, the **S** location (purple dot). Given the anisotropic optical properties of the Au NP dimer, potential hot-spot locations are not confined solely to the gap but may also include the side surfaces of the nanoparticles. Furthermore, in real SERS measurements, the orientations of the Au dimers in the measurement system may exhibit randomness with respect to the polarization direction of the excitation laser. Therefore, investigation on the excitation polarization of the hot-spot becomes crucial. The analyte, we assume to be a large dielectric particle (DP), can also be treated as a sphere with a radius R_D. In principle, the DP can be randomly attached to all the accessible outer surfaces of the dimer, such as **U** or **S**, where $\lambda_{ex} \approx \lambda^{a}_{LSPR}$ & V-polarization or $\lambda_{ex} \approx \lambda^{t}_{LSPR}$ & H-polarization can excite the hot-spot at these contact locations. Among all these possible contact locations, the DP

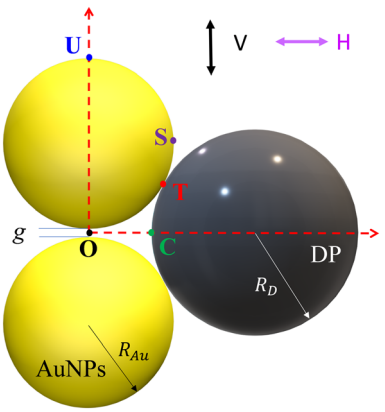

Fig. 1 The Au NP dimer system with a spherical analyte particle.

contacts to both dimer spheres may represent a configuration that most likely to generate the highest SERS signals. The DP and the dimer have two contact points **T** (red dot). In addition, it is likely the location **C** (green dot) on the DP, which is closest to **O** location, may also experience a high local-E-field. The locations **T**, **C**, **S**, and **U** could potentially serve as EHS.

A commercial software package (FDTD Solutions version 8.16.931, Lumerical Solutions Inc.) was used to calculate the localized electric field (E-field) distribution of the AuNP-DP clusters. In the FDTD calculation, R_{Au} = 50 nm, g = 5 nm, R_D varies from 3 nm to 100 nm, with an increment of 10 nm. The dielectric function of the DP is treated as a constant, ε_D = 1.55, and the dielectric functions of Au were taken from Johnson and Christy.[21] The entire structure was surrounded by the dielectric environment of vacuum. Linearly polarized light with the wavelength from 250 nm to 1000 nm was applied, which is consistent with normal SERS measurement configuration. Two polarization directions, *i.e.*, V-polarization and H-polarization, were used in the calculations. Perfectly matched layer (PML) absorbing boundaries were applied in all directions. To ensure the convergence of the calculations, a mesh size of 1 nm × 1 nm × 1 nm was chosen. A monitor of "frequency-domain field profile" was set up to calculate the localized E-field distributions and the obtained E-fields were normalized to the magnitude of the incident E-fields. A MATLAB program was used to extract the *E*-field distribution and the LSPR wavelength results from the FDTD calculations.

3. Results and discussion

Fig. 2 shows the typical local electric field distributions $g_l = |E_{loc}/E_0|^2$ (in logarithmic scale) for the dimer-DP system under λ^b_{LSPR} & V-polarization and under λ^t_{LSPR} & H-polarization for R_D = 0, 5, 25, and 60 nm, respectively. Regardless of the viral particle size, the general trends of the g_l under these two conditions agree well with results from previous publications: at λ^b_{LSPR} & V-polarization, a hot-spot appears at **O** with extremely high g_l (denoted as g_l^{max}), with $g_l^{max} \sim 1.2 \times 10^4$, and $\lambda^b_{LSPR} \approx$ 584–585 nm, which is invariant with R_D. At λ^t_{LSPR} & H-polarization, apparently the g_l distribution is almost invariant at very small R_D (≤5 nm). When R_D = 25 nm, the g_l distribution around the contacts between AuNPs and DP starts to deviate the g_l distribution of the AuNP dimer only case. At R_D = 60 nm, the deviation becomes more serious. Not only much higher local g_l appears around the contacts between AuNPs and DP, but also the local fields penetrate into the DP, which could significantly attenuate the SERS spectral shape (see later distance dependent discussion). The g_l^{max} at **S** is around 17.7–18.7 for $R_D \leq$ 25 nm, while $\lambda^t_{LSPR} \approx$ 550 nm. When R_D = 60 nm, the g_l^{max} at **S** increases significantly, to ~28.5, and λ^t_{LSPR} redshifts to 556 nm. Under this condition, the contact point **T** is very close to **S**.

Though the highest g_l^{max} appears at **O** under λ^b_{LSPR} & V-polarization regardless of the size of DP, this location is inaccessible to DP due to the size exclusion, which means this hot-spot location would play no role to SERS signal of DP. Rather, the locations **T** and/or **C** in Fig. 1 and/or areas around these two locations have the most potentials to contribute to the SERS enhancement, whose g_l^{max} is expected to be significantly smaller than that at **O**. In addition, since these locations really depend on the size of the analyte particle, their g_l shall be size dependent, so should be the corresponding resonant wavelength λ_0^T or λ_0^C, at which the g_l at corresponding locations reach maximum (which will determine how to adjust λ_{ex} to gain the strongest SERS signal). Fig. 3 shows the g_l *versus* λ at **O**, **U**, **T**, **C** for V-polarization (Fig. 3a–c) and **O**, **S**, **T**, **C** for

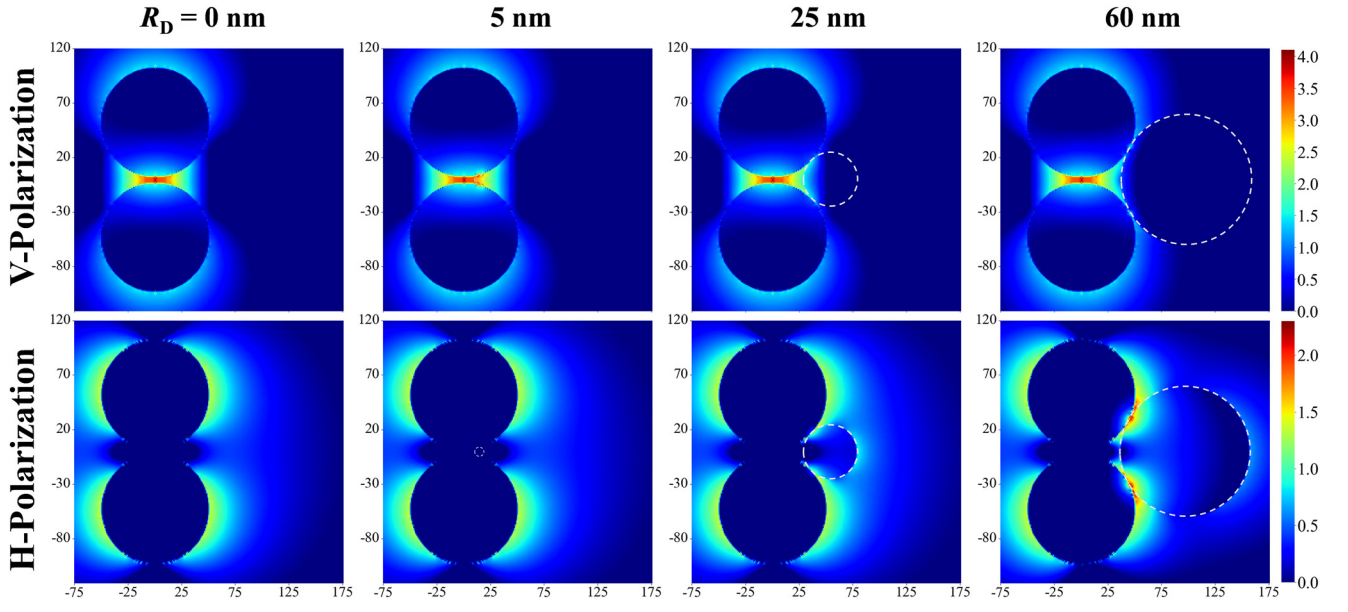

Fig. 2 The local E-field mapping $\log_{10}(g_l)$ at $\lambda^L_{bonding}$ & V-polarization and λ^T & H-polarization for the Au dimer-DP system with R_D = 0, 5, 25, and 60 nm, respectively. The white dashed circles outline the DP.

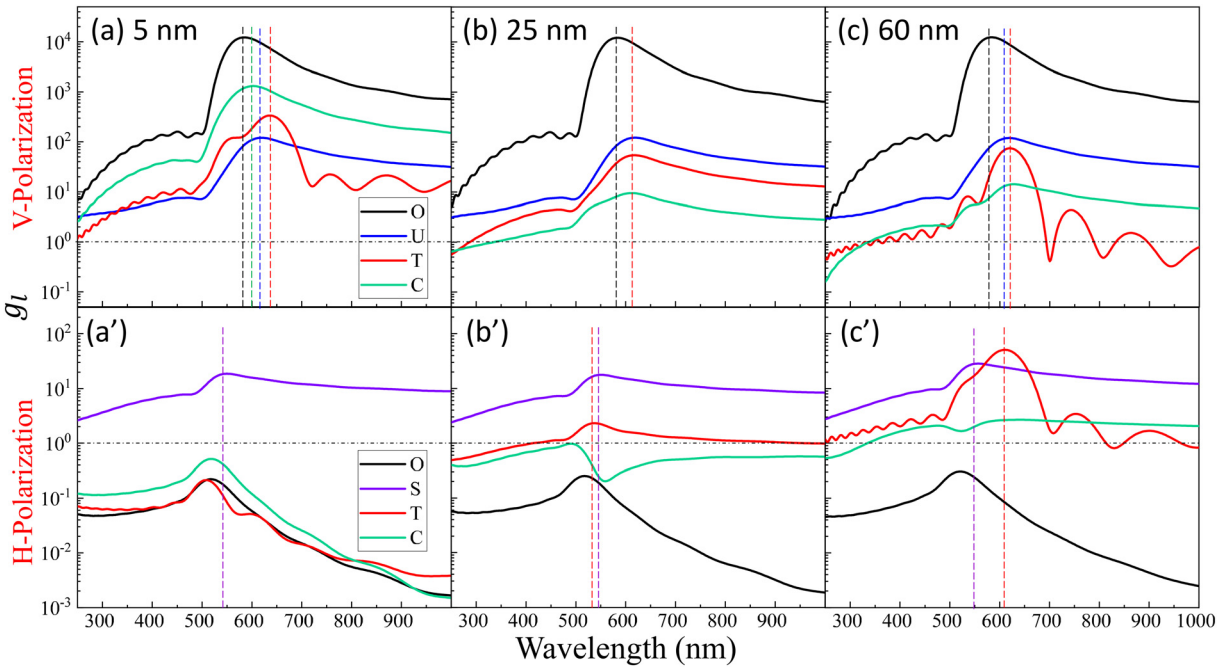

Fig. 3 The plots of g_l *versus* λ at **O**, **U**, **T**, **C** for V-polarization (top row, a–c) and **O**, **S**, **T**, **C** for H-polarization (bottom row, a′–c′) for R_D = 5, 25, and 60 nm, respectively. The vertically colored dashed lines indicate the corresponding λ_0 for the same-colored spectrum.

H-polarization (Fig. 3a′–c′) for R_D = 5, 25, and 60 nm, respectively. The corresponding g_l^{max} and resonance wavelength λ_0 are indicated in the figure with the same color and summarized in Table 1. As can be seen from Fig. 3a–c, for V-polarization, the amplitudes of g_l spectra at other locations are significantly lower than that at **O**, and corresponding λ_0 redshifts with respect to λ^b_{LSPR}, *i.e.*, at **C**, λ_0^C shifts from λ^b_{LSPR} = 585 nm to 602 nm at R_D = 5 nm; then to 618 nm at R_D = 25 nm; and finally to 628 nm at R_D = 60 nm, while g_l^{max} decreases monotonically, from 1.2 × 10^4 to 1312, 54, and 14, respectively. Similarly, λ_0^T changes to 636, 612, and 620 nm while g_l^{max} varies from 336, 9.5, to 75 correspondingly. That is, if the DP is tangent to both dimer spheres, the EHS location, local field strength, and resonant wavelength depend strongly on R_D, *i.e.*, under V-polarization, for $R_D \leq 50$ nm, the EHS for a DP is at **C**; while when R_D = 60 nm, the EHS changes to **T**. However, one shall notice that the g_l^{max} at **U** is almost invariant with R_D, and the λ_0 corresponding to this location is λ^a_{LSPR} = 618–620 nm. It is expected that when a DP is attached to **U** location, it can also serve as an EHS. For H-polarization, a different trend is observed (Fig. 3a′–c′): For a small DP, R_D = 5 nm, at both **C** and **T**, $g_l^{max} < 1$, which means no enhancement of DP can be observed with the configuration shown in Fig. 1, *i.e.*, the EHS is at **S**. However, when R_D increases, to be 60 nm, the g_l^{max} (= 51) at **T** is almost double the value at **S** (= 28.5). The corresponding λ_0 changes to 611 nm, compared to λ^S_{LSPR} 556 nm. Clearly, when

Table 1 The g_l^{max} values and corresponding λ_0 at different locations for V- and H-polarizations for different sized analytes

	Location	No virus	R_D = 5 nm	R_D = 25 nm	R_D = 60 nm
V-Polarization	**T**		336	9.5	75
			636 nm	612 nm	620 nm
	C		1312	54	14
			602 nm	618 nm	428 nm
	U	120	120	122	120
		617 nm	620 nm	618 nm	618 nm
	O	12 658	12 234	12 136	12 402
		584 nm	585 nm	584 nm	584 nm
H-Polarization	**T**		0.21	2.3	51
			508 nm	537 nm	611 nm
	C		0.52	0.97	2.7
			518 nm	490 nm	641 nm
	O	0.22	0.23	0.25	0.31
		517 nm	517 nm	517 nm	521 nm
	S	18.7	18.7	17.7	28.5
		550 nm	550 nm	550 nm	556 nm

DP is large, the EHS location is at **T**. Note that at **O** location, g_1^{max} is always smaller than 1.

The examples above illustrate a strong dependence of both the EHS location and the resonance wavelength λ_0 on the size of DP. To gain a deeper understanding of how both g_1^{max} and λ_0 vary with different positions as a function of R_D, comprehensive FDTD calculations with R_D from 3 nm to 100 nm were performed. The resulting g_1^{max} and λ_0 values *versus* R_D for different positions **O**, **U**, **T**, **C** under V-polarization and **O**, **S**, **T**, **C** under H-polarization are plotted in Fig. 4. In Fig. 4a, under V-polarization, the **O** location consistently exhibits the highest g_1^{max}, varying from 1.20×10^4 to 1.29×10^4, corresponding to the conventional hot-spot. The λ_{LSPR}^{b} only changes slightly, from 583 nm to 595 nm. However, this location is inaccessible for a large DP. An alternative EHS with high g_1^{max} is found at **U**, with g_1^{max} values ranging from 120 to 4 and λ_0 fluctuating between 618 nm and 640 nm. Additionally, **C** and **T** are also identified as EHS locations. At $R_D \leq 15$ nm, both g_1^{max} at **C** (ranging from 2600 to 130) and **T** (ranging from 720 to 58) exceed those at **U**, and the corresponding λ_0 (~600 nm to 612 nm) at **C** is very close to that at **U** while at **T** λ_0 fluctuates from 603 nm to 654 nm. In this R_D region, we can treat the spherical cap formed between **C** and **T** as an EHS area (see Fig. 5a). At $R_D > 15$ nm, g_1^{max} at **U** still is the highest, but **C** and **T** may have comparable strengths. For example, at $15 < R_D \leq 55$ nm, g_1^{max} at **C** (ranging from 73 to 17) surpasses that at **T** (ranging from 17 to 3), but their differences are within one order of magnitude. The corresponding λ_0 varies from 600–630 nm. Similarly, when $55 < R_D \leq 100$ nm, g_1^{max} at **T** (ranging from 75 to 7) is larger than that at **C** (ranging from 14 to 7), while λ_0 fluctuates from 520–620 nm.

Under H-polarization (see Fig. 5b), g_1^{max} at **O** shows the lowest g_1^{max}. At $R_D < 50$ nm, g_1^{max} at **S** is the highest, with almost a constant value (~17–20), while g_1^{max} at **T** increases almost monotonically from 0.5 to 25. At $R_D > 50$ nm, the g_1^{max} at **S** increases gradually to 63 at $R_D = 100$ nm, while g_1^{max} at **T** surpasses the value at **S** in most cases, varying from 30 to 76, with λ_0 primarily varying between 557 and 580 nm. It is worth noting that at **S**, λ_0 changes slightly, varying from 550 nm to 560 nm. This suggests the possibility of two spherical caps between **T** and **S** becoming a potential EHS area (Fig. 5b).

The concept of a EHS area remains applicable even when $R_D > 15$ nm under V-polarization, where the **T** location exhibits the largest g_1^{max}. In spherical coordinates centered at one (top) AuNP in question, the surfaces of entire top half hemisphere (or bottom half hemisphere for the bottom AuNP) displays g_1^{max} values ranging from 10 to 80. Locations closer to **T** exhibit higher g_1^{max} values. Therefore, these hemispheres can be considered as EHS areas. Similarly, for $R_D < 50$ nm under H-polarization, the spherical caps surrounding the **S** locations (of which there are 4) can also be designated as EHS areas.

We notice that regardless of the polarization, the maximum g_1^{max} at various potential EHS locations is consistently around 10^2, and the corresponding λ_0 has relatively substantial variations, ranging from 520 nm to 630 nm, in contrast to the fixed value of 585 nm for the **O** hot-spot. When defining EHS based on locations with the highest g_1^{max}, especially for large DPs, multiple EHS locations may emerge on the SERS substrate or even form an area rather than a single specific point. This property leads to two significant consequences: first, following the principles of SERS, the SERS intensity I_{SERS} can be expressed as

$$I_{SERS} = GF\sigma_{SERS}NI_0, \quad (1)$$

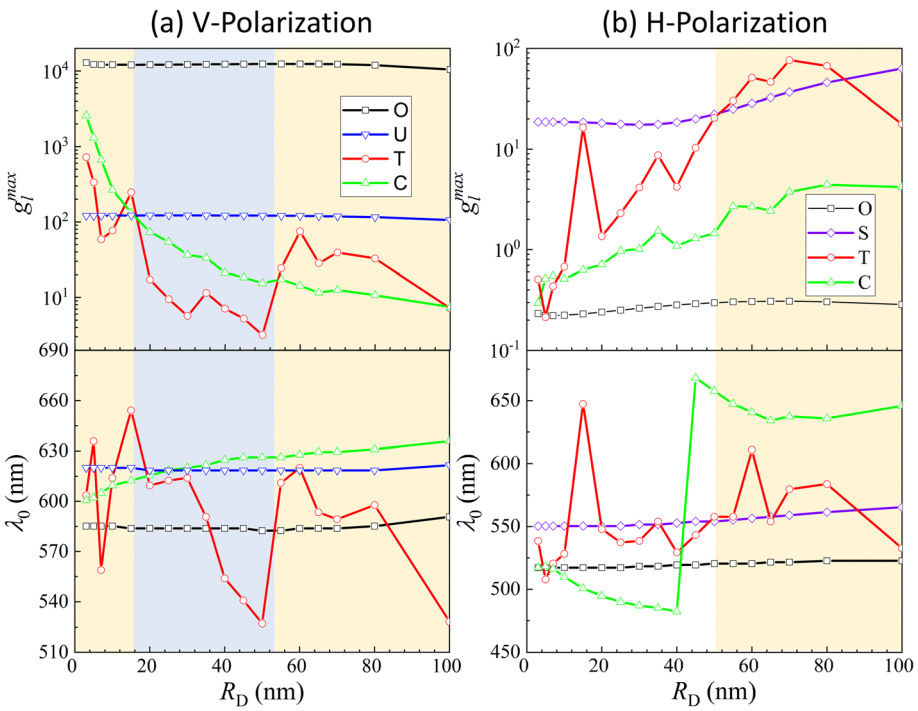

Fig. 4 g_1^{max} and λ_0 as a function of R_D at (a) **O**, **U**, **T**, **C** for V-polarization and (b) **O**, **S**, **T**, **C** for H-polarization.

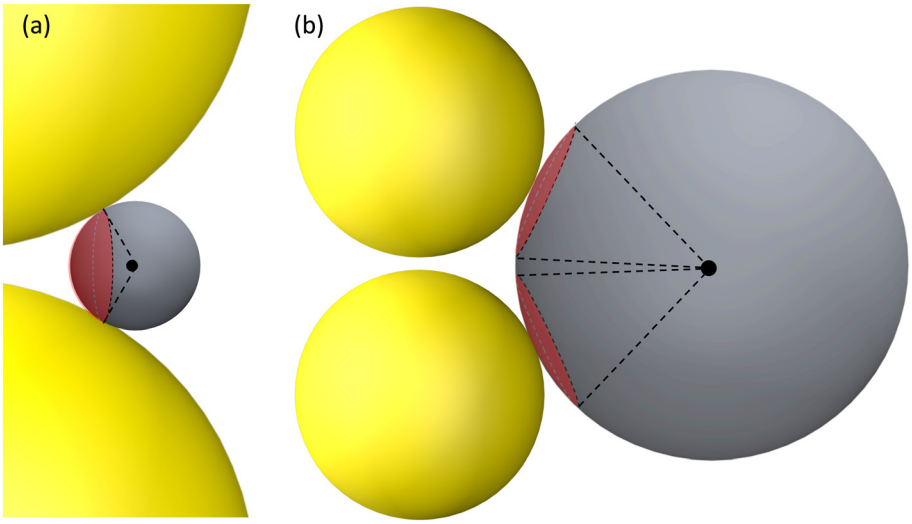

Fig. 5 The hot-spot area on a DP for (a) $R_D \leq 15$ nm and V-polarization and (b) $R_D > 50$ nm and H-polarization. The red spherical caps indicate the possible hot-spot area.

where $G = (g_1^{max})^2$ represents the SERS enhancement factor at the hot-spot/EHS location, F denotes the fraction of photons emitted by analytes within a hot-spot/EHS and collected by the microscopic objective, σ_{SERS} signifies the SERS scattering cross-section of the corresponding analyte, and N stands for the number of analytes adsorbed in a hot-spot/EHS. Despite the decrease in G compared to the conventional hot-spot for larger R_D, the overall surface area of the EHS A_H increases significantly. It is expected that $n \propto A_H$. Thus, as long as the product of $G \times A_H$ remains relatively constant, the SERS intensity could remain relatively stable.

Another crucial observation arises when considering the typical conditions for exciting a conventional hot-spot in AuNP dimers. Such conditions demand strict polarization and resonance wavelength matching. However, with larger-sized analytes, the necessity for stringent polarization conditions might be alleviated. This relaxation is due to the fact that both **U** and **S** locations can act as EHS candidates under various polarization states. These findings suggest a fundamental shift in the designing criteria for SERS substrates when dealing with larger analyte particles. These criteria should be to maximize the local electric fields of locations that are accessible to the analyte particle while simultaneously to optimize the EHS's overall surface area to accommodate larger analyte particles effectively. This, in turn, enhances the potential for successful SERS measurements on larger analyte particles.

Based on above discussion, the EHSs for large DP are not in the location of g_1^{max} where the LSPR wavelength produced (we term this location as traditional hot-spot location). Then some other properties of traditional hot-spot may not hold. One particular property is the distance dependent local field decay. It has been reported that for a spherical particle, $g_1^2 \propto \left(\frac{R}{R+x}\right)^{12}$, where R is the radius of the spherical plasmonic particle, and x is the radial-distance away from the particle surface.[22] Masango *et al.* experimentally measured the distance dependent SERS enhancement factor on bare silver film over nanospheres substrate (AgFON), and demonstrated $g_1^2 \propto C_1\left(\frac{a_1}{a_1+x}\right)^{10} + C_2\left(\frac{a_2}{a_2+x}\right)^{10}$, where a_1 and a_2 are the short-range and long-range radii of curvature of AgFON features, and C_1 and C_2 are related constant.[23] Both situations neglect the analyte particle size effect, *i.e.*, R_D is assumed to be very small compared to the SERS surface features. However, due to the size effect, since both the g_1^{max} and λ_0 change, it is expected that the g_1^2–x relationship can also be altered, which can ultimately affect the interpretation of the SERS spectra.

Based on the above discussion, it is evident that for analytes of varying sizes, location **T** may emerge as the EHS location. The g_1^2–x along the center of one Au NP and the center of the analyte particle is explored, as shown in Fig. 6a. The g_1^2–x relationship for R_D = 25 and 60 nm at both V- and H-polarizations are shown in Fig. 6b. Here x = 0 nm at **T**. The g_1^2–x relationship at O is also plotted to serv as a reference. Compared to the fast decay at **O** location, the g_1^2–x at the contact location **T** shows a much slow decay. In fact, for R_D = 60 nm, we can fit the g_1^2–x using the function $g_1^2 = C\left(\frac{a}{a+x}\right)^n$, and obtain a = 2.5 and 4.6 nm, n = 1.5 ± 0.2 and 1.3 ± 0.1 for V- and H-polarizations, respectively. This implies that the enhancement factor shall follow $g_1^2 \propto C\left(\frac{a}{a+x}\right)^3$ or $C\left(\frac{a}{a+x}\right)^{2.6}$. Such a slow distance-dependent local field can significantly change the interpretation of the SERS spectrum of large analyte particles. If the analyte particle is a virus particle as shown in Fig. 6a, it can be treated as a layered structure at the contact point **T** between the viral particle and the Au NP dimer. For example, if the viral particle is a SARS-CoV-2 or flu virus, at the contact point, the 1st layer consists of pike proteins; the 2nd layer is the viral envelop (lipid bilayer); the

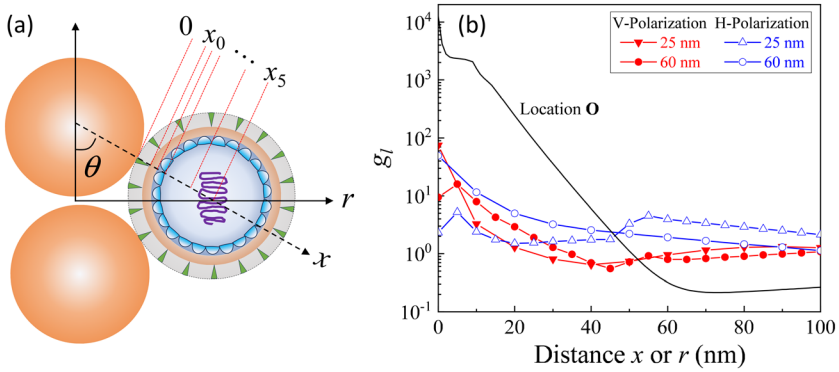

Fig. 6 (a) The layered structure of a virus attached to the Au NP dimer. (b) The distance dependent g_l–x (line + symbol curves) at **T** for V- & H-polarizations, and g_l–r curve at **O** for reference (black curve).

3rd layer is matrix protein; and the 4th or 5th layer comprises of nucleocapsid proteins and RNA.[24] Thus, the SERS intensity can be expressed as,

$$I_{\mathrm{SERS}} \propto \sum_i \int_{x_{i-1}}^{x_i} N_i g_l^2(x)\sigma_i(x)dx. \quad (2)$$

where $g_l(x)$ is the location dependent local field along x-direction shown in Fig. 6b, $\sigma_i(x)$ is the combined SERS scattering cross-section of molecules in ith layer, and N_i is the effective number of the probed molecules in the ith layer. Let $g_l^2 = C\left(\frac{a}{a+x}\right)^n$ and assume that σ_i is independent of x in ith layer, eqn (2) can change to

$$I_{\mathrm{SERS}} \propto \sum_i A_i N_i \sigma_i = \sum_i N_i \sigma_i \int_{x_{i-1}}^{x_i} C\left(\frac{a}{a+x}\right)^n dx, \quad (3)$$

here $A_i = \int_{x_{i-1}}^{x_i} C\left(\frac{a}{a+x}\right)^n dx$ is a linear coefficient depending strongly on a and n according to eqn (3).

$$A_i = C\left(\frac{1}{1+x_{i-1}/a}\right)^n \Delta x_i = g_l^2(x_{i-1})\Delta x_i. \quad (4)$$

Here $\Delta x_i = x_i - x_{i-1} < a$. Clearly the coefficient A_i will determine how much the spectrum from ith layer will contribute to the overall SERS spectrum of the large analyte. It is determined by two critical parameters: a and n. The g_l^2 value approaches more quickly to zero with x/a value for larger n, or in another word, g_l^2 varies slowly with x/a for smaller n. Therefore, for larger analyte particles, since the n value (~2–3) is significantly smaller than that (~10–12) for small analyte molecules, molecules from more layers into the particle need to be considered in order to interpret the resulting SERS spectrum.

While we lack experimental data for virus detection on AuNP-dimers or gap hot-spots, the same principle can be extended to open hot-spot substrates. One example is silver nanorod (AgNR) array substrate made by oblique angle deposition.[15] Our previous work showed that the hot-spots of this substrate were located between the nanorods as well as at the tip of the nanorods. The SERS spectra of various respiratory viruses utilizing AgNR array substrate have been obtained.[25] Fig. 7a show an averaged SERS spectrum of a coronavirus, CoV-NL 63. In the figure, we present the SERS spectra of the virus's key components—the spike protein and RNA—on AgNR substrates, alongside the SERS spectrum of the buffer solution (DMEM) in which the viruses are suspended. According to eqn (2), the SERS spectrum of CoV-NL 63 can be expressed as a linear combination of the SERS

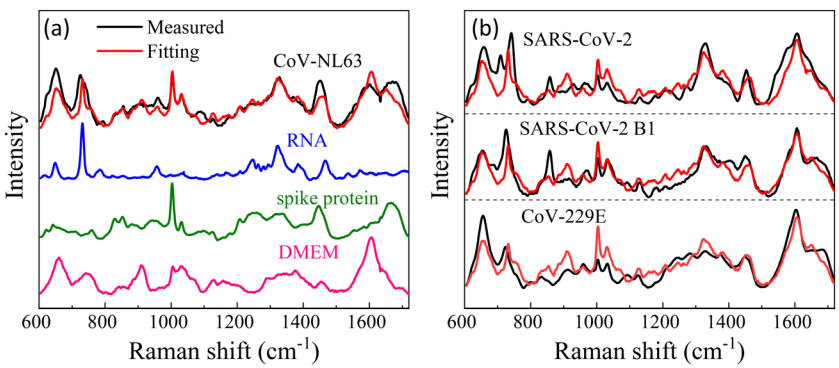

Fig. 7 (a) The experimental SERS spectrum of CoV-NL63, the corresponding SERS spectra of DMEM buffer, spike protein, and RNA. The red curve is the best fitted spectrum of the linear combinations of spike protein, RNA, and DMEM buffer spectra. (b) Comparisons of the experimentally measured virus spectra (black) and fitted spectra (red) using the linear combinations for 3 other coronaviruses.

spectra of DMEM, spike protein, and RNA, *i.e.*, $I_{virus} = dI_{DMEM} + sI_{Spike} + rI_{RNA}$, where d, s, and r are fitting constants. The red curve in Fig. 7a represents the fitted spectrum using above equation, with d = 0.55, s = 0.38, and r = 0.18, respectively. The Pearson's correlation coefficient C_p is about 0.85 between the fitted and experimentally measured spectra. As can be seen from Fig. 7a, nearly all the spectral features in the measured virus spectrum are captured by the fitted spectrum. Notably, the r value is approximately half of the s value, indicating substantial contributions from RNA. Similar data analysis can be conducted for other coronaviruses, as shown in Fig. 7b for CoV-229E, SARS-CoV-2 B1, SARS-CoV-2, HMPV-B with d = 0.74, 0.63, 0.72, s = 0.35, 0.31, 0.2, r = 0.13, 0.17, 0.2, and C_p = 0.83, 0.82, 0.81, respectively. In all cases, $d > s \geq r$. The larger contribution from DMEM is understandable because the buffer contains small biomolecules that can easily access normal hot-spot locations. Yet, for all the fittings, r is about half of the s or even the same. All these results suggest that the sharp distance dependent relationship for G may not be applicable for the detection of large analytes.

Though the investigations here are focused on NP dimers, the conclusions drawn from the dimer shall be very general and are applicable for other gap hot-spot configurations such as clusters and NP on a film. The analysis of size effects on the Au NP dimer yields several significant findings, especially when the size of the analyte is sufficiently large: firstly, the EHS shall be defined as the region where the analyte particle attaches to the SERS substrate with the highest local electric field. Secondly, the resonance frequency/wavelength to excite this EHS location can exhibit notable shifts compared to this to excite the original gap hot-spot. Thirdly, both the EHS location and resonant frequency exhibit strong dependencies on the size of the analytes. Moreover, the relationship of distance-dependent EF for SERS undergoes substantial modifications, with components inside the analyte particle potentially contributing significantly to the measured SERS spectra. These conclusions are anticipated to be applicable to other gap hot-spot configurations with slight modifications, as certain configurations may be complicated. For instance, in NP clusters with multiple gaps, the field enhancements at different gap locations could vary. Notably, studies have shown that the middle gap in a gold NP tetramer chain structure had the highest electromagnetic enhancement among the three gaps,[26] while calculations by Ding *et al.* suggested a distribution of electromagnetic enhancements in gaps of clusters made of multiple NPs.[27] Consequently, when an analyte particle is situated near different gap locations, the effective EF and change in optical property are anticipated to differ. Particularly in scenarios where the number of NPs in a cluster is substantial but the number of analyte particles attached to the cluster is minimal, the optical properties of the cluster may not undergo significant changes, yet the EF and distance-dependent SERS effects may be altered markedly. Similar arguments can be extended to third-generation hot spots.

4. Conclusions

In summary, our study explored the impact of analyte particle size on the gap hot-spot within the Au NP dimer system for a SERS substrate. Our findings reveal a strong dependence between the EHS location, where the local E-field reaches its maximum, and the resonant wavelength necessary to achieve this local E-field, on the size of the analyte particle. Interestingly, the local E-field strength can be considerably weaker than the conventional gap hot-spot when excited at the LSPR wavelength. And the resonant wavelength for these intensified local E-fields can significantly shift, either red- or blue-shifted, in comparison to the LSPR wavelength.

In the specific case of the Au NP dimer configuration, the EHS predominantly occurs at the contact point between the Au NP and the analyte particle. This EHS can cover a larger area than the conventional hot-spot and is excitable at various polarizations. Moreover, these changes impact the distance-dependent relationship of the local E-field, leading to a much slower decay compared to the conventional hot-spot scenario. Consequently, interpreting the SERS spectrum of large analyte particles needs consideration of molecular compositions from the outer surface to the inner contents, offering richer information for discrimination and quantification.

Our results imply two key considerations: first, for large analyte particles, since the location of the EHS, enhancement factor, and resonance wavelength all change with analyte particle size, SERS substrate design rules should be size-dependent. To achieve the highest EF, the SERS substrate's accessible surfaces for analyte particles should align with the maximum local E-fields, and for SERS measurements, the excitation laser should closely match the resonance wavelength of the EHS' accessible area.

Secondly, interpreting the SERS spectrum of large analyte particles might be intricate, but the spectrum can be tuned to better represent the analyte particle's unique molecular characteristics. The maximum local field enhancement and distance effects change based on the SERS nanostructure, incident polarization, and analyte size. To enhance classification and quantification, particularly for microorganisms with distinctive internal molecular features, adjusting the power index n of the g_1^2–x relationship to a smaller value allows multiple layers of the analyte to contribute to the spectra. We anticipate that our findings will pave the way for innovative SERS substrate designs tailored for large analyte particles.

Declaration of generative AI and AI-assisted technologies in the writing process

During the preparation of this work the authors used ChatGPT in order to proof-write the manuscript, *i.e.*, to get rid of possible grammar errors and change the sentence structures. After using this tool/service, the authors reviewed

and edited the content as needed and take full responsibility for the content of the publication.

Author contributions

Y. Y.: FDTD calculations, data analysis, writing – review & editing. Xinyi Chen: MATLAB code for data analysis. Bin Ai: writing – review & editing. Y. Z.: conceptualization, data analysis, funding acquisition, supervision, project administration, writing – original draft, writing – review & editing.

Conflicts of interest

The authors declare that they have no known competing financial interests or personal relationships that could have appeared to influence the work reported in this paper.

Acknowledgements

Y. Y. and Y. Z. are funded by USDA NIFA Grant number 2023-67015-39237.

References

1 Y. Wang, *Principles and Clinical Diagnostic Applications of Surface-Enhanced Raman Spectroscopy*, Elsevier, 2022.
2 J. Langer, D. Jimenez de Aberasturi, J. Aizpurua, R. A. Alvarez-Puebla, B. Auguié, J. J. Baumberg, G. C. Bazan, S. E. J. Bell, A. Boisen, A. G. Brolo, J. Choo, D. Cialla-May, V. Deckert, L. Fabris, K. Faulds, F. J. García de Abajo, R. Goodacre, D. Graham, A. J. Haes, C. L. Haynes, C. Huck, T. Itoh, M. Käll, J. Kneipp, N. A. Kotov, H. Kuang, E. C. Le Ru, H. K. Lee, J.-F. Li, X. Y. Ling, S. A. Maier, T. Mayerhöfer, M. Moskovits, K. Murakoshi, J.-M. Nam, S. Nie, Y. Ozaki, I. Pastoriza-Santos, J. Perez-Juste, J. Popp, A. Pucci, S. Reich, B. Ren, G. C. Schatz, T. Shegai, S. Schlücker, L.-L. Tay, K. G. Thomas, Z.-Q. Tian, R. P. Van Duyne, T. Vo-Dinh, Y. Wang, K. A. Willets, C. Xu, H. Xu, Y. Xu, Y. S. Yamamoto, B. Zhao and L. M. Liz-Marzán, *ACS Nano*, 2020, **14**, 28–117.
3 S.-Y. Ding, E.-M. You, Z.-Q. Tian and M. Moskovits, *Chem. Soc. Rev.*, 2017, **46**, 4042–4076.
4 A. Shiohara, Y. Wang and L. M. Liz-Marzán, *J. Photochem. Photobiol., C*, 2014, **21**, 2–25.
5 S. Shanmukh, L. Jones, J. Driskell, Y. P. Zhao, R. Dluhy and R. A. Tripp, *Nano Lett.*, 2006, **6**, 2630–2636.
6 F. Saviñon-Flores, E. Méndez, M. López-Castaños, A. Carabarin-Lima, K. A. López-Castaños, M. A. González-Fuentes and A. Méndez-Albores, *Biosensors*, 2021, **11**, 66.
7 P. A. Mosier-Boss, *Biosensors*, 2017, **7**, 51.
8 L. Mikac, I. Rigó, L. Himics, A. Tolić, M. Ivanda and M. Veres, *Appl. Surf. Sci.*, 2023, **608**, 155239.
9 Q. Chen, J. Wang, F. Yao, W. Zhang, X. Qi, X. Gao, Y. Liu, J. Wang, M. Zou and P. Liang, *Microchim. Acta*, 2023, **190**, 465.
10 B. Alberts, A. Johnson, J. Lewis, M. Raff, K. Roberts and P. Walter, *Molecular biology of the cell*, Garland Science/Taylor & Francis LLC, New York, 4th edn, 2002.
11 *Medical Microbiology*, ed. S. Baron, The University of Texas Medical Branch at Galveston, Galveston, 4th edn, 1996.
12 P. A. Levin and E. R. Angert, *Cold Spring Harbor Perspect. Biol.*, 2015, **7**, a019216.
13 E. Uurasjärvi, S. Hartikainen, O. Setälä, M. Lehtiniemi and A. Koistinen, *Water Environ. Res.*, 2020, **92**, 149–156.
14 Y. Zhao, *Nanomaterials*, 2023, **13**, 2998.
15 Y. Zhao, A. Kumar and Y. Yang, *Chem. Soc. Rev.*, 2024, **53**, 1004–1057.
16 R. Rastogi, E. A. Dogbe Foli, R. Vincent, P.-M. Adam and S. Krishnamoorthy, *ACS Appl. Mater. Interfaces*, 2021, **13**, 9113–9121.
17 J. Liu, G. Xu, X. Ruan, K. Li and L. Zhang, *Front. Environ. Sci. Eng.*, 2022, **16**, 143.
18 C. E. Talley, J. B. Jackson, C. Oubre, N. K. Grady, C. W. Hollars, S. M. Lane, T. R. Huser, P. Nordlander and N. J. Halas, *Nano Lett.*, 2005, **5**, 1569–1574.
19 K. D. Alexander, M. J. Hampton, S. Zhang, A. Dhawan, H. Xu and R. Lopez, *J. Raman Spectrosc.*, 2009, **40**, 2171–2175.
20 N. Zohar, L. Chuntonov and G. Haran, *J. Photochem. Photobiol., C*, 2014, **21**, 26–39.
21 P. B. Johnson and R.-W. Christy, *Phys. Rev. B: Solid State*, 1972, **6**, 4370.
22 R. Aroca, *Surface-Enhanced Vibrational Spectroscopy*, John Wiley & Sons, Ltd, Chichester, England, 2006.
23 S. S. Masango, R. A. Hackler, N. Large, A.-I. Henry, M. O. McAnally, G. C. Schatz, P. C. Stair and R. P. Van Duyne, *Nano Lett.*, 2016, **16**, 4251–4259.
24 M. Y. Wang, R. Zhao, L. J. Gao, X. F. Gao, D. P. Wang and J. M. Cao, *Front. Cell. Infect. Microbiol.*, 2020, **10**, 587269.
25 Y. J. Yang, B. B. Xu, J. Murray, J. Haverstick, X. Y. Chen, R. A. Tripp and Y. P. Zhao, *Biosens. Bioelectron.*, 2022, **217**, 114721.
26 P. A. Mercadal, J. C. Fraire and E. A. Coronado, *J. Phys. Chem. C*, 2022, **126**, 10524–10533.
27 S.-Y. Ding, J. Yi, J.-F. Li, B. Ren, D.-Y. Wu, R. Panneerselvam and Z.-Q. Tian, *Nat. Rev. Mater.*, 2016, **1**, 16021.